RSC Advances

PAPER

View Article Online
View Journal | View Issue

Cite this: *RSC Adv.*, 2021, **11**, 30980

Welding partially reduced graphene oxides by MOFs into micro–mesoporous hybrids for high-performance oil absorption†

Lu Sun and Jun Tang *

Partially reduced graphene oxides (PRGOs) with a small number of COOH groups remaining at the edges were interlocked by UiO-66-NH_2 nanoparticles into hierarchical porous hybrids (PRGO@UiO-66-NH_2) during the synthesis of UiO-66-NH_2 in the presence of PRGOs, in which the UiO-66-NH_2 nanoparticles provide micropores and the interlocked PRGO skeletons provide mesopores. The peak intensity of the functional groups on the PRGO@UiO-66-NH_2 hybrids decrease greatly when compared with the GO@UiO-66-NH_2 hybrids and the UiO-66-NH_2 nanoparticles, and the number of –COOH at the edge of the PRGOs are approximately 6.3% after reduction, which is confirmed by the FT-IR and XPS results. When the PRGO@UiO-66-NH_2 hybrids were embedded in their macropores *via* hydrogen bonding, melamine foams (MFs) were able to effectively absorb a variety of water-immiscible organic solvents from oil/water biphasic mixtures and, at the same time, suppress water infusion due to Cassie-state surface superhydrophobicity with a water contact angle of 154.2° in air. After 10 cycles, the PRGO@UiO-66-NH_2-laden MFs exhibited water contact angles of 148.3°, which indicated that the composite MFs had excellent stability and recycling ability after 10 cycles. The PRGO@UiO-66-NH_2-laden MFs had an oil absorption capacity of >10 000 wt% of the dry mass of absorbents and water absorption capacity of ≈1.76 wt% of the adsorbate, thus highlighting the high absorption selectivity of oil over water.

Received 23rd July 2021
Accepted 6th September 2021

DOI: 10.1039/d1ra05644a

rsc.li/rsc-advances

1 Introduction

An oil spill is an example of an anthropogenic disaster with a long-term, severe impact on public health, the environment, and the economy of local communities, in particular where it takes place.[1–3] Nowadays small and regular improper disposal of oil into aquatic ecosystem occurs on a regular basis because of the massive amount of transportation of oil across oceans and land, and the increasing use of oil-propelled automobiles. Because of the escalating growth of offshore oil drilling and extraction to meet to the insatiable oil demand worldwide, the occurrence of large-scale oil spills, such as that which happened in the Mexico Gulf in 2010,[4] will increase in frequency in the coming years. In addition to traditional methods such as floatation, distillation, solvent extraction and ultrafiltration with large equipment footprints, in recent years there has been rapid development of advanced nanostructured absorbents with a high absorption capacity for oil.[5–7] The prevailing oil absorbent design is built on hierarchical porous structures with fairly oleophilic porous surfaces, which are able to not only be readily wetted by oil for effective oil permeation[8–10] but also make the surfaces of the porous structures as a whole, superhydrophobic with water contact angles ($\theta_{w/a}$) above 150°, which are associated with a large fraction of air trapped in the pores according to the Cassie–Baxter equation.[5] The combination of the overall structural surface superhydrophobicity and the surface oleophilicity of individual pores is not easily implemented using conventional polymer sponges or inorganic porous structures coated with low surface energy molecules.[11,12]

In past decades, the progress in materials' science and engineering in preparing oil absorbents is largely driven by two classes of advanced materials, graphene-related and graphene-like two dimensional nanomaterials and metal–organic frameworks (MOFs). In the graphene family, graphene oxides (GOs) rapidly emerge as unique adsorbents thanks to their (quasi-) monolayered non-polar planes of hexagonally arranged carbon atoms with abundant OH groups, and especially COOH groups at edges, which are available for further functionalization.[13–15] The MOFs are known as microporous crystalline coordination structures with a high surface area, high porous volume, and high structural stability[16–20] and have been extensively exploited as building blocks to functionalize macroporous skeletons by direct growth on the interior macroporous surfaces of polymer sponges[21,22] and self-assembly with the aid of polymers[23] and inorganic nanoparticles.[24–26] An increasing amount of effort has recently been devoted to amalgamating GOs and MOFs into hierarchical porous composites with the aim of joining their

Department of Polymer Science, Jilin University, Changchun 130012, China. E-mail: chemjtang@jlu.edu.cn

† Electronic supplementary information (ESI) available. See DOI: 10.1039/d1ra05644a

unique structural and chemical properties into one composite.[27–29] The MOFs can be induced to grow on the surface of GOs by coordination with the metal in the MOFs precursor or by electrostatic attraction. In general, there are two main approaches to synthesizing MOFs and GO composites. One is that the synthesized MOF materials are dispersed in a GO dispersion and the GO@MOF composites are synthesized by electrostatic attraction or a dispersion force. However, the interaction between GOs and MOF materials is weak, which leads to uneven particle mixing. The other is to disperse GOs in the MOF precursor solution, and use the coordination effect between the functional groups on the GO surface and the metal ions to induce the growth of MOFs on the GO surface. In this method, the interaction between the GO and the MOF materials is strong, and the template effect of GO can be used to guide the formation and distribution of MOF particles. Fischer and co-workers recently integrated highly fluorinated GOs and ZIF-8 into a superhydrophobic foam for oil/water separation.[30] Because the abundant edge polar groups of GO are beneficial for covalent or non-covalent binding with MOFs to form porous hybrids, they also make the surfaces of the resulting hybrids fairly hydrophilic, thus facilitating infusion of water, which results in poor absorption selectivity of oil over water in applications for oil absorption. Apart from the GOs and MOFs composites, recently reduced GOs (RGOs) and MOF composites have also been fabricated and found to endow better hydrophobicity with the aid of other materials, which leads to more complicated operations in the material preparation process. After reduction of GOs by $NaBH_4$, the resulting RGOs become noticeably hydrophobic but less reactive than GOs due to the loss of COOH groups at the edges.[31] Thus, the fully reduced RGOs can barely form strong interactions with the active groups on MOFs and foams,[32,33] which may cause difficulties for the adsorption and recovery of crude oil, especially limiting the durability of oil absorbing materials in practical application.

Herein, a simple and effective approach is introduced for preparing a 3D foam of partially reduced GOs (PRGOs) combined with Zr-based MOF-UiO-66-NH_2, which unites the challenging needs of superhydrophobicity and structure stability in a single platform. The critical step is that hydriodic acid (HI) was used instead of $NaBH_4$ to reduce the GOs, which yielded PRGOs with a small number of COOH groups remaining at the edge.[34,35] When the as-prepared PRGOs were introduced into the reaction media for the synthesis of amine-functionalized UiO-66-NH_2, the remaining COOH groups at the edge of the PRGOs were able to form strong coordination bonding with the surface Zr^{4+} sites of newly grown UiO-66-NH_2 nanoparticles to form micro–mesoporous hybrids, denoted as PRGO@UiO-66-NH_2. Because of the noticeable hydrophobicity of the PRGOs, the resulting PRGO@UiO-66-NH_2 hybrids can effectively repel water. The PRGO@UiO-66-NH_2 hybrids were tightly coated onto the macroporous surfaces of the MFs as a result of hydrogen bonding between the former and latter NH_2 groups. The resulting PRGO@UiO-66-NH_2-laden MFs exhibited an outstanding absorption performance for a broad range of water-immiscible organic solvents, with an absorption capacity in the range of 4900–10 000 wt% and, at the same time, they possessed Cassie-state superhydrophobic surfaces with a water contact angle in air ($\theta_{w/a}$) of 154.2°, and so were able to effectively inhibit the permeation of water into the MFs, and thus ensured a high oil-to-water absorption ratio as high as 50. This universal method of preparing oil-absorbing foams will lead the way for new marine crude oil recovery and water treatment methods.

2 Results and discussion

2.1 Preparation of micro–mesoporous hybrids

The UiO-66-NH_2 was chosen for use in the present study because its surface Zr^{4+} sites were capable of forming strong coordination bonds with the COOH groups on the edges of the PRGOs, and the NH_2 groups of its struts were capable of forming hydrogen bonds with the interior macroporous surfaces of the MFs. According to a modified protocol previously reported in the literature,[36] the UiO-66-NH_2 nanoparticles with sizes of about 50 nm were easily produced *via* a 24 h incubation of the mixtures of $ZrCl_4$ and 2-amino-1,4-benzenedicarboxylic acid (ABDCA) in *N*,*N*-dimethylformamide (DMF) at 120 °C under stirring (Fig. S1, ESI†). Using a modified Hummers' method,[37] GOs were produced *via* oxidation-driven exfoliation of graphite flakes, which were found to be uniform ultrathin sheets (Fig. S2a, ESI†) which possessed abundant COOH groups at the edge, as revealed by X-ray photoelectron spectroscopy (XPS) (Fig. S3a, ESI†). When the synthesis of UiO-66-NH_2 was carried out in the presence of GOs, the growing UiO-66-NH_2 nanoparticles were expected to 'stitch' the edges of the GOs together by coordination between the COOH groups on the GO edge and the Zr^{4+} sites of the UiO-66-NH_2 nanoparticles. The GO@UiO-66-NH_2 hybrids were expected to be noticeably hydrophilic, which would be a recognizable technical difficulty for the design of oil absorbents with highly selective absorption of oil over water. However, after the GOs were reduced by $NaBH_4$,[38] the resulting hydrophobic RGOs had few COOH groups left at the edge, and thus could hardly form hybrids with the UiO-66-NH_2 nanoparticles. To circumvent this, here HI was utilized as the reducing agent to produce the PRGOs.[35] Whereas the HI reduction caused little change in morphology between the GOs and the PRGOs (Fig. S2b, ESI†), the fraction of the GO carbon in the form of COOH was reduced from 57.7% for GOs to 6.3% for PRGOs (Fig. S3, ESI†). Because of the small number of COOH groups still remaining at the edges, the resulting PRGOs were expected to interact with UiO-66-NH_2 nanoparticles in a way similar to the GOs. To further verify how the number of carboxyl groups changes, Fourier-transform infrared spectroscopy (FT-IR) was applied to determine the content of remaining active groups after reduction by HI (Fig. S4a, ESI†). The concentration of HI was adjusted from 15.7–55 wt% to determine the content of hydroxyl groups on the PRGOs after reduction with different concentrations of HI. The FT-IR spectrum shows that the bending vibration absorptions at 1086 cm^{-1}, 1360 cm^{-1} and 3600–3800 cm^{-1} were attributed to the hydroxyl groups at the edge of the PRGOs. The bending bands at approximately 1730–1690 cm^{-1} were assigned to the C=O on the carboxyl groups and the change of absorption peak

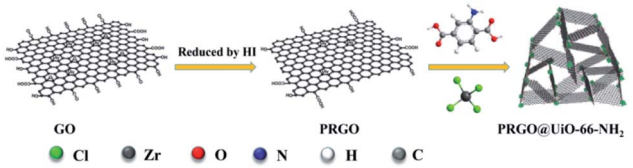

Scheme 1 Schematic illustration of the synthesis of PRGO@UiO-66-NH_2 hybrids.

position comes from the influence of the hydrogen bonds. The characteristic vibrational signals at 1620 cm^{-1} should be the C═O on the GOs. The bending bands at approximately 1436 cm^{-1} and 900 cm^{-1} were attributed to the hydroxyl groups from the carboxyl groups. It was obvious that all of the peak intensities decreased gradually with the decrease of the concentration of HI. Therefore, to give the composites strong hydrophobicity for the high-performance oil absorption, the PRGOs treated with 55 wt% HI were chosen as the next target for our research. In addition, the PRGO@UiO-66-NH_2 hybrids were also characterized by FT-IR. As for the PRGO@UiO-66-NH_2 hybrids, the intensity of the characteristic peaks at 1150 cm^{-1} (stretching vibration of –OH), 1490 cm^{-1} and 960 cm^{-1} (bending vibration of –OH on –COOH) and 1560 cm^{-1} (N–H bending band) were reduced greatly when comparing to those of UiO-66-NH_2 and GO@UiO-66-NH_2 hybrids, indicating that a small number of COOH groups remaining at the edges were interlocked by the UiO-66-NH_2 nanoparticles (Fig. S4b, ESI†). In particular, when the synthesis of UiO-66-NH_2 was carried out in the presence of PRGOs, the newly growing UiO-66-NH_2 nanoparticles were expected to bind the PRGOs together into PRGO@UiO-66-NH_2 hybrids *via* coordination of the former surface Zr^{4+} sites with the COOH groups on the edge of the latter (Scheme 1).

Fig. 1 shows that there was little difference in morphology between the resulting PRGO@UiO-66-NH_2 and GO@UiO-66-NH_2 hybrids, whereas their color reflected the combination of the constituent UiO-66-NH_2 nanoparticles (Fig. S1, ESI†) and GOs or PRGOs (Fig. S2, ESI†). The scanning electron microscopy (SEM) imaging showed that both GO@UiO-66-NH_2 and PRGO@UiO-66-NH_2 hybrids were obtained as large flat aggregates, whereas either individual UiO-66-NH_2 nanoparticles, GOs or PRGOs ultrathin sheets were hardly visible (Fig. 1a, b, S5 and S6, ESI†). Transmission electron microscopy (TEM) images revealed that the ultrathin sheets of GOs or PRGOs were densely bound with UiO-66-NH_2 nanoparticles (Fig. 1c and d). Meticulous XPS analysis indicated that the PRGO@UiO-66-NH_2 hybrids had less nitrogen content, and that the signal arose solely from the UiO-66-NH_2 nanoparticles, rather than the GO@UiO-66-NH_2 hybrids (Fig. S7 and Table S1, ESI†). This reflected the fact that the PRGOs had much fewer COOH groups at edge available for complexation with the surface Zr^{4+} sites of the UiO-66-NH_2 nanoparticles than the GOs (Fig. S7, ESI†).

The powder X-ray diffraction (XRD) patterns of the as-prepared GO@UiO-66-NH_2 and PRGO@UiO-66-NH_2 hybrids revealed peaks at 7.6°, 12.2°, 25.8° and 43.5°, which are characteristic of UiO-66-NH_2, thus confirming that there was little impact, by the GOs or PRGOs on the coordination of the Zr^{4+} ions and ABDCA, on the crystallinity of the resulting UiO-66-NH_2 framework (Fig. 2). The mean lattice size (d) of the UiO-66-NH_2 nanoparticles formed in the resulting hybrids can be estimated according to Scherrer eqn (1):

$$d = \kappa\lambda/\beta \cos\theta \quad (1)$$

where κ is 0.89, λ is 0.154 nm, β and θ are the full width at half maximum and the angle of Bragg diffraction peaks, respectively. The d values of the UiO-66-NH_2 nanoparticles formed in the GO@UiO-66-NH_2 and PRGO@UiO-66-NH_2 hybrids were about 37.7 nm and 31.4 nm, respectively, which were comparable with each other but slightly smaller than the d values of UiO-66-NH_2 nanoparticles obtained in the absence of GOs or PRGOs (42.3–46.6 nm). Note that there was a way to convert as-prepared GO@UiO-66-NH_2 hybrids into PRGO@UiO-66-NH_2 *via* HI reduction, however, this caused noticeable damage to the crystalline framework of the UiO-66-NH_2 nanoparticles obtained, and the characteristic diffraction peaks of the UiO-66-NH_2 nanoparticles were hardly visible (Fig. S8, ESI†).

The nitrogen sorption assessment revealed that the as-prepared UiO-66-NH_2 nanoparticles exhibited a type-I

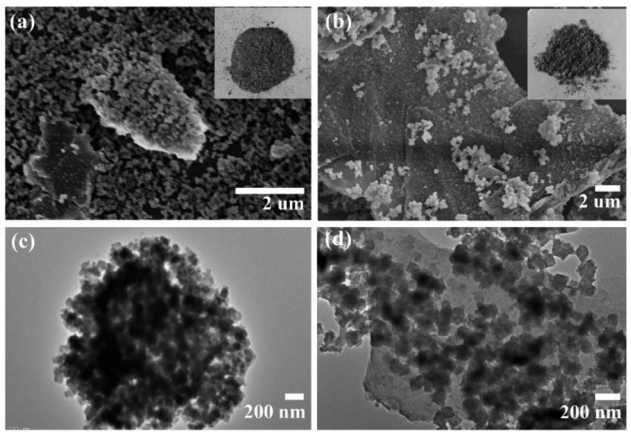

Fig. 1 The SEM (a, b) and TEM (c, d) images of the as-prepared GO@UiO-66-NH_2 (a, c) and PRGO@UiO-66-NH_2 hybrids (b, d). The insets in (a) and (b) are the images of the powders of the as-prepared GO@UiO-66-NH_2 and PRGO@UiO-66-NH_2 hybrids, respectively.

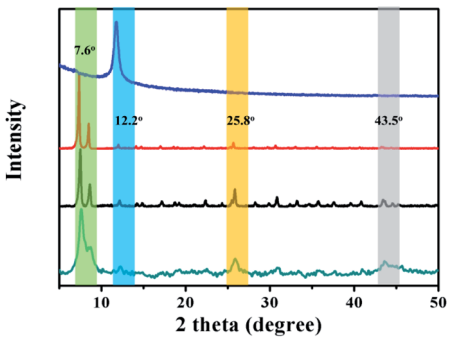

Fig. 2 The XRD patterns of the as-prepared GO (blue curve), UiO-66-NH_2 nanoparticles (red curve), GO@UiO-66-NH_2 hybrids (black curve) and PRGO@UiO-66-NH_2 hybrids (green curve).

isotherm which is characteristic of microporous materials, whereas the resulting GO@UiO-66-NH_2 and PRGO@UiO-66-NH_2 exhibited both type I and type IV isotherms (Fig. 3a), in which the narrow hysteresis loops at the relative pressure (P/P_0) in the range of 0.8–1.0 for the GO@UiO-66-NH_2 hybrids and 0.4–0.6 for the PRGO@UiO-66-NH_2 hybrids signified the coexistence of micropores and mesopores (Fig. S9, ESI†).[30] The pore size distributions of the resulting samples in the microporous and mesoporous regions were analyzed by Horvath–Kawazoe (HK) and Barrett–Joyner–Halenda (BJH) methods, respectively. The UiO-66-NH_2 nanoparticles obtained in the absence of GOs or PRGOs had micropores in the size range of 0.5–1.5 nm. The GO@UiO-66-NH_2 and PRGO@UiO-66-NH_2 hybrids displayed both micropores and mesopores. The former micropores (*ca.* 1.25 nm) were slightly larger than the latter (*ca.* 0.97 nm), whereas the large fraction of the former mesopores (*ca.* 3.60 nm) was slightly smaller than that of latter (*ca.* 3.92 nm). This may be a reflection of the fact that the number of COOH groups on the edge of the PRGO was noticeably smaller than that of the GOs, so after being interlocked by the UiO-66-NH_2 nanoparticles, the PRGOs may aggregate into more loosely packed mesoporous structures than the GOs. It should be noted that the micropores sizes of the as-prepared GO@UiO-66-NH_2 and PRGO@UiO-66-NH_2 hybrids fall in the size range of the mesopores of the UiO-66-NH_2 nanoparticles obtained in the absence of GOs or PRGOs. This implied that the micropores of the resulting hybrids were attributed to the UiO-66-NH_2 nanocrystals bound between the GOs or PRGOs. The Brunauer–Emmett–Teller method was applied to the surface areas of the as-prepared GO@UiO-66-NH_2 and PRGO@UiO-66-NH_2 hybrids (Fig. S10, ESI†). When compared with the surface area (966.8 m^2 g^{-1}) of the microporous UiO-66-NH_2 nanoparticles obtained in the absence of GOs or PRGOs, those of the micro–mesoporous hybrids were noticeably reduced, and the surface area of the GO@UiO-66-NH_2 hybrids was 669.1 m^2 g^{-1} and that of the PRGO@UiO-66-NH_2 hybrids was 693.4 m^2 g^{-1}. These results indicated that the surface Zr^{4+} sites of the UiO-66-NH_2 nanoparticles with the COOH groups on the edges of the GOs or PRGOs, resulted in a big loss in surface porosity of the UiO-66-NH_2 nanoparticles, and the loss in the surface area is expected to be larger than that of GOs with more –COOHs on their edges than the PRGOs.

In order to determine the influence of different ratios on the pore size of composite materials, the composites were synthesized with different ratios (20 : 20 : 15.5 and 1 : 20 : 15.5) of GOs/PRGOs, $ZrCl_4$ and ABDCA. The XRD patterns of the as-prepared hybrids with the ratio of 1 : 20 : 15.5 revealed the presence of peaks at 7.6°, 12.2°, 25.8° and 43.5°, which were similar to those obtained for UiO-66-NH_2, thus confirming that was little impact of the GOs or PRGOs on the coordination of Zr^{4+} ions to form crystals (Fig. 4a). However, for the composites of GOs/PRGOs, $ZrCl_4$ and ABDCA with the ratio of 20 : 20 : 15.5, it was obvious that excessive powders of GOs and PRGOs prohibited the formation of the framework of the MOFs. Nitrogen sorption experiments were also made to reveal the pore size distribution as shown in Fig. 4b–f. The composites of GOs/PRGOs, $ZrCl_4$ and ABDCA with the ratio of 20 : 20 : 15.5 had mesopores in the range of 2–4 nm, whereas the composites of GOs/PRGOs, $ZrCl_4$ and ABDCA with the ratio of 1 : 20 : 15.5 only had micropores, and when compared with the GO@UiO-66-NH_2 and PRGO@UiO-66-NH_2 hybrids they had both micropores and mesopores as mentioned previously. The excessive $ZrCl_4$ and ABDCA would not coordinate with the remaining carboxyl groups on PRGOS, but tended to form MOFs first because of the great disparity of the quantity of active groups, thus forming a microporous structure, and indicating that the necessary conditions for the formation of microporous and mesoporous structures is related to the ratio of the GOs/PRGOs, $ZrCl_4$ and ABDCA.

2.2 Preparation of micro–meso–macroporous foams

In order to exploit the applicability of the as-prepared PRGO@UiO-66-NH_2 hybrids in oil absorption, and especially to determine the impact of their surface wettability on the absorption selectivity of oil over water, commercially available macroporous MFs, shown in Fig. S11 (ESI†), were utilized as hosts to load the as-prepared UiO-66-NH_2 nanoparticles, GO@UiO-66-NH_2 hybrids and PRGO@UiO-66-NH_2 hybrids, because the NH_2 groups on the macroporous surfaces of the

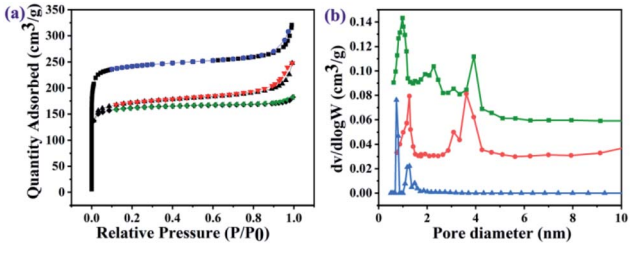

Fig. 3 Nitrogen sorption isotherms (a) and pore size distribution profiles (b) of as-prepared UiO-66-NH_2 nanoparticles (blue curves), GO@UiO-66-NH_2 hybrids (red curves) and PRGO@UiO-66-NH_2 (green curves).

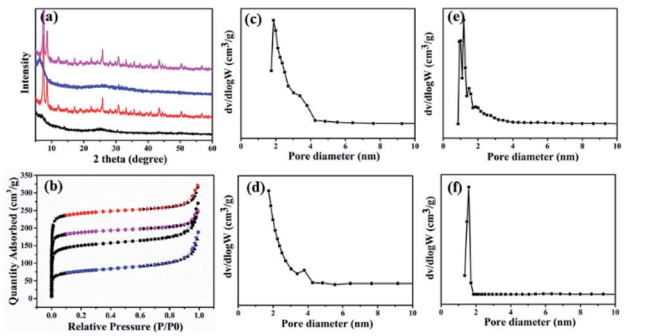

Fig. 4 The XRD patterns (a) and nitrogen sorption isotherms (b) of GOs, $ZrCl_4$ and ABDCA hybrids with ratios of 20 : 20 : 15.5 (black curve), GOs, $ZrCl_4$ and ABDCA hybrids with ratios of 1 : 20 : 15.5 (red curve), PRGOs, $ZrCl_4$ and ABDCA hybrids with ratios of 20 : 20 : 15.5 (blue curve) and PRGOs, $ZrCl_4$ and ABDCA hybrids with ratios of 1 : 20 : 15.5 (pink curve). The pore size distribution profiles of GOs, $ZrCl_4$ and ABDCA hybrids with ratios of 20 : 20 : 15.5 (c), PRGOs, $ZrCl_4$ and ABDCA hybrids with ratios of 20 : 20 : 15.5 (d), GOs, $ZrCl_4$ and ABDCA hybrids with ratios of 1 : 20 : 15.5 (e), and PRGOs, $ZrCl_4$ and ABDCA hybrids with ratios of 1 : 20 : 15.5 (f).

MFs were expected to form hydrogen bonds with the NH_2 groups of the UiO-66-NH_2 nanoparticles to secure the loading stability. It should be noted that since their edge OH and COOH groups were also expected to form hydrogen bonds with the NH_2 groups on the macroporous surfaces of MFs, GOs and PRGOs, they could adsorb onto the MFs in a similar way with UiO-66-NH_2 nanoparticles. After loading, the color of the MF hosts changed from white to a color which was largely dependent on the color of the loaded porous guests (Fig. 5a). Their macroporous structures remained hardly changed with the macroporous surfaces noticeably coated by the functional guests (Fig. 5b, c and S12, ESI†). Energy dispersive X-ray spectroscopy (EDS) mapping further substantiated the uniform surface coverage of the PRGO@UiO-66-NH_2 hybrids on the macropores of the MFs (Fig. 5d). To prove the chemical composition of the composite MFs, the FT-IR spectrum was used to prove the chemical composition of the composite MFs.

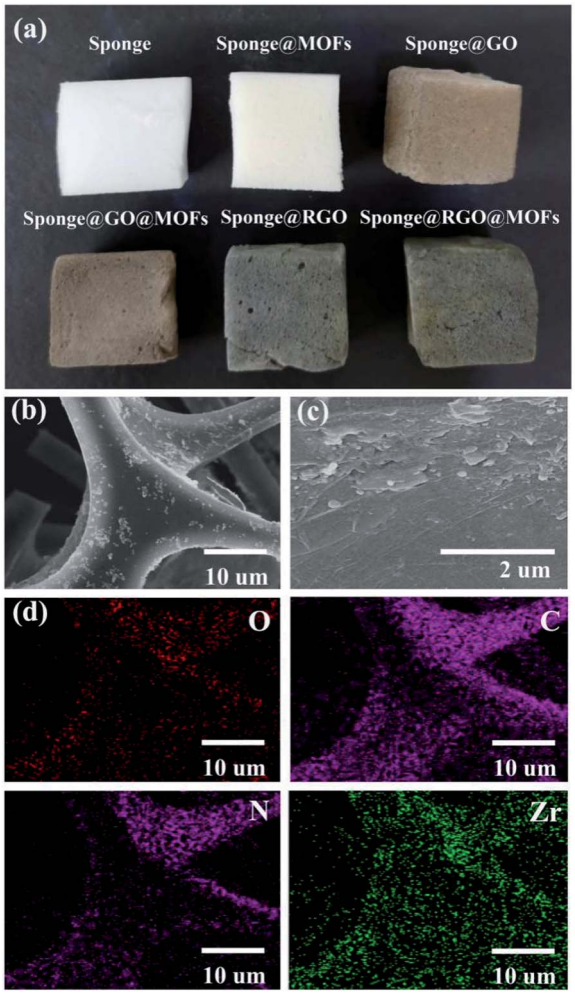

Fig. 5 (a) Images of a block of pristine MF and the blocks of the composite MFs loaded with as-prepared UiO-66-NH_2 nanoparticles, GOs and GO@UiO-66-NH_2 hybrids, PRGOs, and PRGO@UiO-66-NH_2 hybrids. Low (b) and high (c) magnification SEM images of as-prepared PRGO@UiO-66-NH_2-laden MFs, and (d) the EDS elemental mapping of the C, N, O and Zr elements positioned on the macropores.

As shown in Fig. S13 (ESI†), the pristine MFs loaded onto the GOs and PRGOs exhibited similar characteristic peaks at 3360 cm^{-1}, 1550 cm^{-1}, 1440 cm^{-1} and 1320 cm^{-1} due to the existence of the amine groups. The apparent new peak at approximately 970 cm^{-1} was attributed to the carboxyl groups at the edge of the GOs/PRGOs. As for the UiO-66-NH_2-laden MFs, the GO@UiO-66-NH_2-laden MFs and the PRGO@UiO-66-NH_2-laden MFs, there was a new peak which appeared at 1650 cm^{-1} and the peak intensity increased greatly at 3360 cm^{-1}, which was due to the introduction of the –NHCO on UiO-66-NH_2 nanoparticles.

A moderately hydrophobic solid is both hydrophobic and oleophilic as a result of its surface energy being smaller than the surface tension of water but larger than that of oil.[8] The wetting behavior of a solid surface can be noticeably altered provided there are nanostructures molded on the surface according to Wenzel[39] and the Cassie–Baxter equations.[10] To enhance the oil absorption efficiency and absorption selectivity of oil over water in particular, being able to engineer surface wettability is considered to be the core of novel design of oil absorbents.[4] The as-prepared UiO-66-NH_2 nanoparticles and GO or PRGO ultrathin sheets, on the macropores of MFs slightly amplified the surface roughness at the nanoscale, whereas their hybrid micro–mesopore introduced nanostructured textures on the surfaces of the MF macropores, which was expected to significantly amplify the surface hydrophobicity as a result of air entrapment in the nanostructures, provided the nanostructured surface was reasonably hydrophobic according to the Cassie–Baxter model.[8,40] This accounts for the fact that macroporous MFs loaded with PRGOs or PRGO@UiO-66-NH_2 hybrids were able to float well on the surface of water due to the hydrophobicity of PRGOs (Fig. 6e and f). In contrast, the coating of UiO-66-NH_2 nanoparticles, GOs, and GO@UiO-66-NH_2 was deemed to be sufficiently hydrophilic for effective water wetting, which was the rationale behind the fact that the MFs loaded by these guests readily position themselves underneath the surface of water (Fig. 6b–d).

To study the water repellence of the as-prepared composite MFs, water wetting on the foam surfaces in air was measured using the sessile drop method. While the water readily penetrated into pristine MFs with an apparent water contact angle in

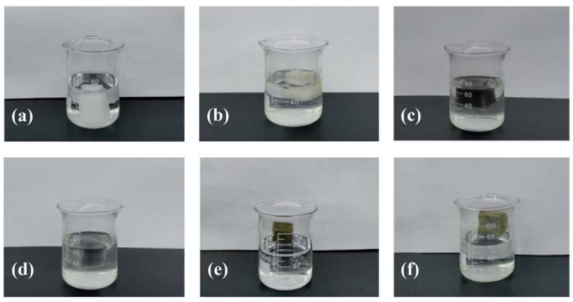

Fig. 6 Images of a block of pristine MF (a) and the blocks of the composite MF loaded with UiO-66-NH_2 nanoparticles (b), GO (c), GO@UiO-66-NH_2 hybrids (d), PRGO (e), and PRGO@UiO-66-NH_2 hybrids (f), placed in water in a beaker.

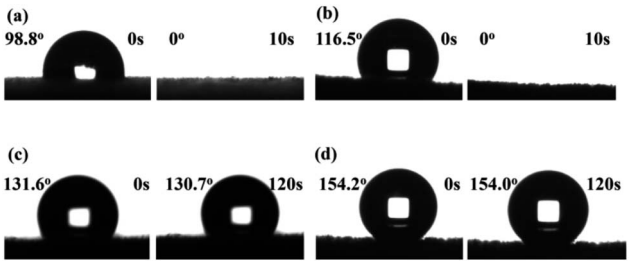

Fig. 7 Temporal shape evolution of the water droplets (2 μL) on MFs loaded with GOs (a), GO@UiO-66-NH_2 hybrids (b), PRGOs (c), and PRGO@UiO-66-NH_2 hybrids (d) in air. The images are taken immediately after the water droplets are placed on the MF surfaces (left panels) and after 10 s in (a) and (b), and at 120 s in (c) and (d) (right panels). The corresponding $\theta_{w/a}$ values and storage times are marked in the images.

air ($\theta_{w/a}$) of 0° (Fig. S14, ESI†), the composite MFs loaded with GOs or GO@UiO-66-NH_2 hybrids display apparent $\theta_{w/a}$ of 98.8° and 116.3°, respectively, immediately after 2 μL water droplets were placed on top of the MF surfaces (Fig. 7a and b), which was due to air trapping in the mesoporous structures of the GOs and GO@UiO-66-NH_2 coatings. However, these large apparent $\theta_{w/a}$ values rapidly dropped to zero within 10 s, which was indicative of rapid water penetration into the mesoporous coatings on the composite MFs due to the fairly hydrophilic nature of the GOs (Fig. 7a and b). In stark contrast, composite MFs loaded with PRGOs and PRGO@UiO-66-NH_2 hybrids exhibited stable apparent $\theta_{w/a}$ over 120 s of storage in air, and the former $\theta_{w/a}$ is 131.6° (Fig. 7c) and the latter $\theta_{w/a}$ is 154.2° (Fig. 7d). The apparent surface superhydrophobicity of PRGO@UiO-66-NH_2-laden MFs was expected to enhance the absorption selectivity of oil over water. On the other hand, the oil readily penetrated the PRGO@UiO-66-NH_2-laden MFs once it had been placed on top of the MF, and the apparent oil contact angle in air ($\theta_{o/a}$) was 0° (Fig. S15, ESI†). In order to determine the hydrophobicity and the stability of the PRGOs-laden MFs after reduction with different concentrations of HI, and the composites of PRGO@UiO-66-NH_2-laden MFs, the water repellence of the as-prepared MFs was studied using the sessile drop method. It was observed that the hydrophobicity of the composite MFs was significantly improved when the concentration of HI increased leading to the increase in stability of the composite MFs (Table S2, ESI†). The integration of excellent oil permeation and water repellence in one, therefore means that the PRGO@UiO-66-NH_2-laden MFs are promising oil absorbents.

2.3 Assessment of the oil absorption performance of PRGO@UiO-66-NH_2-laden MF

The absorption capacity (η_l) of the absorbent for a liquid (l) is calculated by eqn (2):[30]

$$\eta_l = (M_w^l - M_d)/M_d \times 100\% \quad (2)$$

where M_d is the mass of the absorbent used and M_w^l the absorbent mass obtained after absorption of a targeted liquid (l). In this research, both the absorption capacities of pristine MFs and composite MFs for oil and water, were assessed. Fig. 8a shows that pristine MFs and composite MFs loaded with UiO-66-NH_2 nanoparticles displayed a higher absorption capacity for water than for oil, whereas composite MFs loaded with GOs, GO@UiO-66-NH_2 hybrids, PRGOs, and PRGO@UiO-66-NH_2 hybrids showed that the absorption capacities for oil were higher than those of water. The absorption capacity of water was significantly reduced as the hydrophobicity of the loaded guests was increased. Out of all the absorbents used in this work, the pristine MFs exhibited the highest absorption capacity of water (η_{water} of *ca.* 12 098 wt%) with substantial oil absorption of η_{oil} of *ca.* 10 053 wt%, whereas the MFs loaded with the PRGO@UiO-66-NH_2 hybrids exhibited the highest absorption capacity of oil (η_{oil} of *ca.* 10 537 wt%) with a negligible absorption of water (η_{water} of *ca.* 176 wt%). Fig. 8b shows that there was nearly a complete blockage of water penetration into the PRGO@UiO-66-NH_2-laden MFs, which was evidenced by the barely visible fluorescence of rhodamine B after incubation in rhodamine-stained water. The fluorescence of rhodamine B remained barely visible for PRGO-laden MFs after incubation in the dye solution.

Fig. 9 shows that PRGO@UiO-66-NH_2-laden MFs can not only rapidly absorb oil from water within a few seconds but can also easily discharge the absorbed oil by simple squeezing and is then ready for reuse. In the current study it was demonstrated

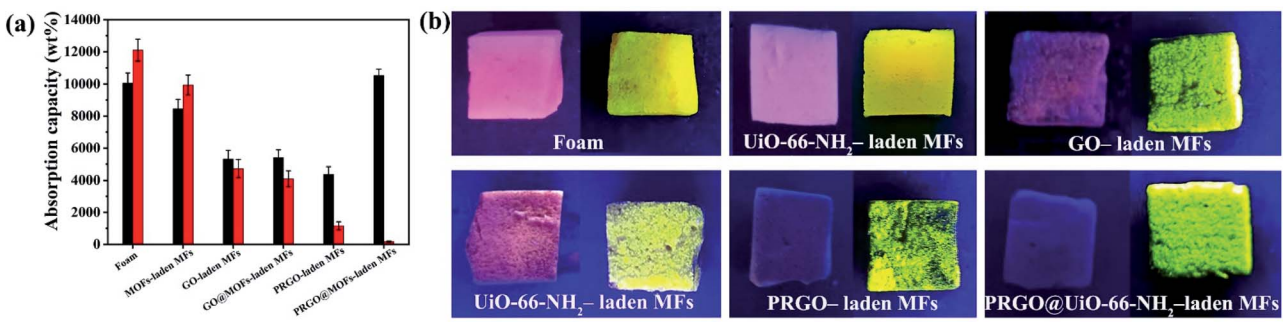

Fig. 8 (a) Summary of the absorption capacities of pristine MFs and composite MFs loaded with UiO-66-NH_2 nanoparticles, GOs, GO@UiO-66-NH_2 hybrids, PRGOs and PRGO@UiO-66-NH_2 hybrids for vegetable oil (black bars) and water (red bars). (b) Images, taken under a UV lamp, of pristine and composite MFs after their absorption of rhodamine B-stained water (left foams) and Nile Red-stained oil (right foams).

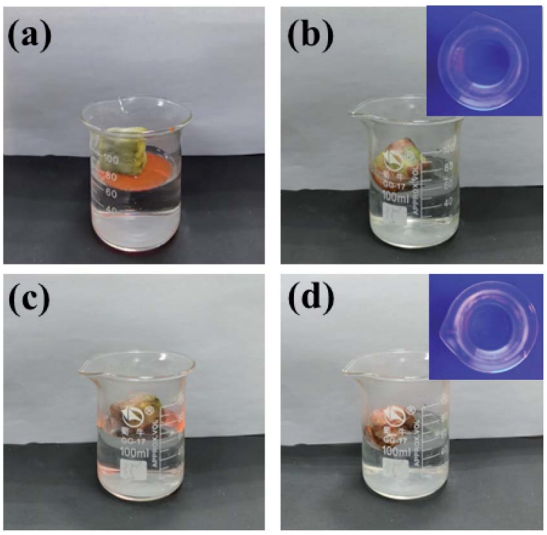

Fig. 9 A series of images taken after a composite MF block loaded with PRGO@UiO-66-NH_2 hybrids was placed on top of an oil/water biphasic mixture (a), and the MF completely absorbed the oil layer spilt on the water surface within 5 s (b), and then after the absorbed oil was squeezed out, the same composite MF block was placed on a new oil/water biphasic mixture (c) and was able to completely absorb the oil layer from the water surface within 5 s (d). The oil phase was vegetable oil (VO) stained with Nile Red. After oil absorption by the composite MF block, the fluorescence of the Nile Red was barely visible (b and d).

that the MFs could be re-used at least 10 times without noticeable loss in absorption capacity and selectivity. To prove the excellent, recyclability of the PRGO@UiO-66-NH_2-laden MFs after 10 cycles of oil adsorption and water repellence, the water contact angles in air of the PRGO@UiO-66-NH_2-laden MFs after 10 cycles were measured. As shown in Fig. S16 (ESI†), the PRGO@UiO-66-NH_2-laden MFs displayed stable apparent $\theta_{w/a}$ of 154° before oil absorption (Fig. S16a, ESI†), which was close to the apparent $\theta_{w/a}$ of 148.3° after 10 cycles (Fig. S16b, ESI†), which indicated that the PRGO@UiO-66-NH_2-laden MFs still exhibited surface superhydrophobicity and had excellent recyclability after 10 cycles. As comparison, GO@UiO-66-NH_2-laden MFs could absorb the majority but not all of oil from water, and a small amount of oil remained floating on the water (Fig. S17, ESI†). This was attributed to the foams positioning themselves underneath the water surface, and their significant absorption of water and the concomitant leakage of water due to gravity. Fig. 10a shows that PRGO@UiO-66-NH_2-laden MFs were able to readily absorb not only VO but also a variety of organic solvents, ranging from hexane, toluene (Tol), dichloromethane, and chloroform (CF), with negligible solubility for diethyl ether (DE), petroleum ether (PE), and ethyl acetate (EA) with tiny but non-negligible solubility in water, and the oil absorption capacity was in the range of 4900 wt% to 10 000 wt%. Whereas the evaporation of absorbed organic solvents, especially in the case of hexane (Hex) and diether ether may account for an apparent small oil absorption capacity, the oil phase can be reasonably effectively trapped within the hierarchical porous structures of PRGO@UiO-66-NH_2-laden MFs, as evidenced by the strong fluorescence of Nile Red after absorption of Nile Red stained organic solvents from water (Fig. 10b). As a reference, the oil absorption ability of various novel existing materials whose hydrophobicity and oil absorption performance are the top 15 so far were compared with the PRGO@UiO-66-NH_2-laden MFs fabricated in the research reported in this paper. From Table 1, it can be observed that except for the superhydrophobicity of these novel materials, all of them exhibit excellent superoleophilicity. Because of the superhydrophobicity due to the micro–mesoporous structure, the PRGO@UiO-66-NH_2-laden MFs could absorb oil from more than 10 types of organic solvents or oil/water mixtures, and places it among the top three of the existing absorbent materials. It is worth noting that the absorption capacity of the PRGO@UiO-66-NH_2-laden MF was superior to those reported in the literature. Except for the intrinsic hydrophobicity of the PRGOs, the micro–mesoporous structure endowed the materials with high pore volumes and high stability which are beneficial to the high oil absorption capacity under the synergistic action of hydrophobic materials and the micro–mesoporous structure. Furthermore, the NH_2 groups on the surfaces of the composite MF can form hydrogen bonds with the NH_2

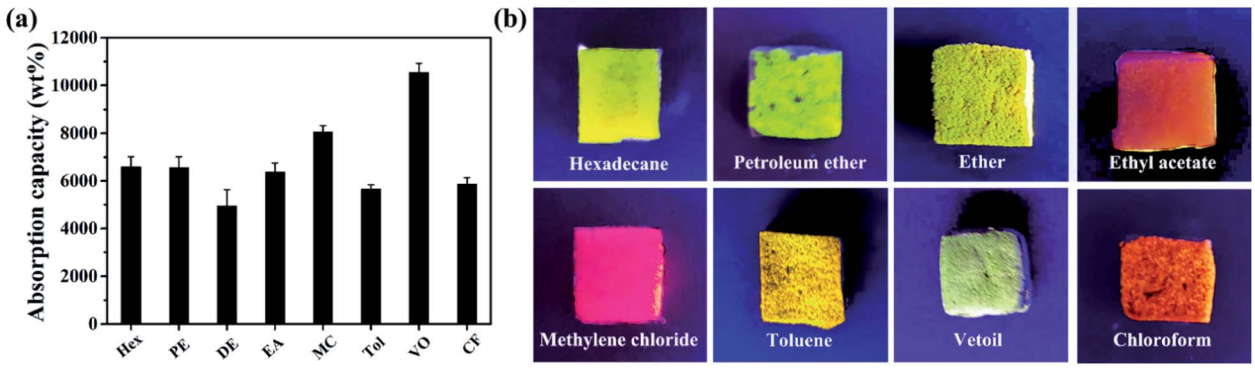

Fig. 10 (a) Summary of the absorption capacities obtained using PRGO@UiO-66-NH_2-laden MFs for a variety of organic solvents (black bars), ranging from hexane (Hex), petroleum ether (PE), diethyl ether (DE), ethyl acetate (EA), methylene chloride (MC), toluene (Tol), vegetable oil (VO), chloroform (CF) after they are placed in oil/water biphasic mixtures. (b) Images of PRGO@UiO-66-NH_2-laden MFs after absorption of Nile Red stained organic solvents. The organic solvents used are marked in the images.

Table 1 Comparison of the oil absorption performance of the present PRGO@UiO-66-NH_2-laden MFs with that of the oil absorbents reported in literature in the past decade

Oil absorbents	Preparation methods	$\theta_{w/a}$ (°)	$\theta_{o/a}$ (°)	Oil species used for absorption	Absorption capacity (×100%)	Recycle ability	Ref.
MOF@rGO sponges	Self-assembles and dip coating	171	0	Chloroform, toluene ethyl acetate, acetone, silicon oil, bean oil, benzinoform, *n*-heptane	14–29	Good	27
Conjugated microporous polymers coated sponges	Dip-coating after homocoupling polymerization	167	0	Vegetable oil, pump oil, octane, dodecane, decane, hexane, phenol, THF, nitrobenzene, chloroform, DMF, 1,2-dichlorobenzene, ethylbenzene, toluene, benzene, DMSO, acetone, ethanol, methanol	6–23	Good	41
Amine-functionalized SiO_2/PTFE coated PU sponges	Chemical vapor deposition after dip coating procedure	165	0	*n*-Hexane, pentane, heptane, benzene, toluene, silicone oil	10–12	Fair	42
Boron nitride nanosheets	Templating approach	165	0	Ethanol, toluene, pump oil, used engine oil, ethylene glycol	20–33	Good	43
CNT-coated meshes	Thermal chemical vapor deposition	163 ± 4	0	Emulsion (diesel, lubricating oil)	n.a.	Good	44
Polyester fabrics coated with DA-TiO_2 and SiO_2	Dip-coating on polyester fabric	158	0	Hexadecane	n.a.	Good	45
P_2VP-*b*-PDMS coated meshes	Grafting from then dip-coating	157.2	0	Gasoline, lubricating oil	n.a.	Good	46
Spiropyran-containing methacrylate	Copolymerization after solution immersion	155 ± 27	n.a.	Silicon oil, pump oil, gasoline, dichloromethane, hexane, DMF, chloroform	70–154	Good	47
PRGO@UiO-66-NH_2-laden MFs	***In situ* synthesis of UiO-66-NH_2 in the presence of PRGOs**	**154**	**0**	**Dichloromethane, hexane, DMF, chloroform, vegetable oil, ether, ethylacetacte, toluene, petroleum ether**	**84.5–110.4**	**Good**	**This work**
Polyester fabrics coated with HFA-TiO_2 and SiO_2	Dip-coating on polyester fabric	152	151	Hexadecane, soybean oil, paraffin oil, diesel	n.a.	Fair	48
ZIF-8/carbon nitride foam	Fast graphitization and coating	135	0	Pentane, petroleum ether, hexane, isopropyl ether, decane, ethanol, pump oil, THF, NMP, dichloromethane, chloroform, ethylene glycol	55–136	Fair	49
PNIPAM	*In situ* polymerization on nylon membranes	120 ± 30	0	Emulsion, hexane, toluene, lubricating oil, gasoline	4.6	Good	50

groups of the UiO-66-NH_2 nanoparticles which secured the loading stability, which was an advantage to improving the recyclability of the PRGO@UiO-66-NH_2-laden MFs. The stable entrapment of oil within the PRGO@UiO-66-NH_2-laden MFs should offer additional technical benefits to oil removal, because it effectively suppressed the leakage of the oil absorbed therein.

3 Conclusions

In summary, high-performance 3D foams for use in oil absorption were demonstrated, prepared by a novel strategy utilizing UiO-66-NH_2 nanoparticles to weld PRGOs into micro–mesoporous hybrids, where the micropores arise from the periodic frameworks of the resulting UiO-66-NH_2 nanoparticles and the mesopores are formed as a result of the UiO-66-NH_2 locked aggregation of the PRGOs. After the PRGO@UiO-66-NH_2 hybrids were loaded into the macropores of the MF *via* hydrogen bonding, the whole surface of the resulting composite MFs became superhydrophobic and effectively resistant against penetration of water through the foams. As a result, the present PRGO@UiO-66-NH_2-laden MFs displayed excellent absorption performance for a variety of organic solvents with negligible or poor water solubility in water and ultrahigh absorption selectivity of oil over water. Their oil absorption capacity can be as high as 10 000 wt%, whereas that of water is only ≈1.76 wt% with all the adsorbates tested, which is comparable to the best oil absorption performance of oil absorbents found in literature so far (Table 1). Because of its ease of operation, this approach will lead to new prospects in the development of oil absorbents and, hopefully, stimulate more ingenious design of PRGO@-MOF hybrids by taking advantage of the wide spectrum of MOFs currently available to further enhance the oil absorption performance. Furthermore, this work also demonstrates that although they have very few COOH groups at the edge (as low as 6% of carbon), the PRGOs can be readily conjugated with functional nanomaterials in a similar way to how GOs do, which therefore integrates the chemical flexibility of GOs and the

physicochemical properties of RGOs in one. As a result, it is hoped that the results of this research will increase the awareness of PRGOs as a promising alternative to RGOs in technical applications especially in catalysis, electrochemical energy storage, electronics, and solar cells.

Conflicts of interest

There are no conflicts to declare.

Acknowledgements

This work was supported by the Science and Technology Development Project of Science and Technology Department of Jilin Province (No. 20180201086GX).

References

1 E. Barry, J. A. Libera, A. U. Mane, J. R. Avila, D. DeVitis, K. Van Dyke, J. W. Elam and S. B. Darling, *Environ. Sci.: Water Res. Technol.*, 2018, **4**, 40–47.
2 M. A. Shannon, P. W. Bohn, M. Elimelech, J. G. Georgiadis, B. J. Mariñas and A. M. Mayes, *Nature*, 2008, **452**, 301–310.
3 R. Das, C. D. Vecitis, A. Schulze, B. Cao, A. F. Ismail, X. Lu, J. Chen and S. Ramakrishna, *Chem. Soc. Rev.*, 2017, **46**, 6946–7020.
4 Z. Xu, K. Miyazaki and T. Hori, *Adv. Mater. Interfaces*, 2015, **2**, 1500255.
5 J. Ge, H. Y. Zhao, H. W. Zhu, J. Huang, L. A. Shi and S. H. Yu, *Adv. Mater.*, 2016, **28**, 10459–10490.
6 H. Guan, Z. Y. Cheng and X. Q. Wang, *ACS Nano*, 2018, **12**, 10365–10373.
7 C. L. Yu, C. M. Yu, L. Y. Cui, Z. Y. Song, X. Y. Zhao, Y. Ma and L. Jiang, *Adv. Mater. Interfaces*, 2017, **4**, 1600862.
8 Z. L. Chu, Y. J. Feng and S. Seeger, *Angew. Chem., Int. Ed.*, 2015, **54**, 2328–2338.
9 S. Li, J. Huang, Z. Chen, G. Chen and Y. Lai, *J. Mater. Chem. A*, 2017, **5**, 31–55.
10 Q. Ma, H. Cheng, A. G. Fane, R. Wang and H. Zhang, *Small*, 2016, **12**, 2186–2202.
11 M. Tao, L. Xue, F. Liu and L. Jiang, *Adv. Mater.*, 2014, **26**, 2943–2948.
12 Y. Zhu, J. Wang, F. Zhang, S. Gao, A. Wang, W. Fang and J. Jin, *Adv. Funct. Mater.*, 2018, **28**, 1804121.
13 D. Li and R. B. Kaner, *Science*, 2008, **320**, 1170–1171.
14 D. Wu, F. Zhang, H. Liang and X. Feng, *Chem. Soc. Rev.*, 2012, **41**, 6160–6177.
15 H. P. Cong, J. J. He, Y. Lu and S. H. Yu, *Small*, 2010, **6**, 169–173.
16 A. Huang, W. Dou and J. Caro, *J. Am. Chem. Soc.*, 2010, **132**, 15562–15564.
17 S. Horike, S. Shimomura and S. Kitagawa, *Nat. Chem.*, 2009, **1**, 695–704.
18 H. Furukawa, K. E. Cordova, M. O'Keeffe and O. M. Yaghi, *Science*, 2013, **341**, 1230444.
19 J. K. M. Eddaoudi, N. Rosi, D. Vodak, J. Wachter, M. O'Keeffe and O. M. Yaghi, *Science*, 2002, **295**, 469–472.
20 J. L. C. Rowsell and O. M. Yaghi, *Microporous Mesoporous Mater.*, 2004, **73**, 3–14.
21 Z. Lei, Y. Deng and C. Wang, *J. Mater. Chem. A*, 2018, **6**, 3258–3263.
22 D. Kim, D. W. Kim, O. Buyukcakir, M.-K. Kim, K. Polychronopoulou and A. Coskun, *Adv. Funct. Mater.*, 2017, **27**, 1700706.
23 T. Kitao, Y. Zhang, S. Kitagawa, B. Wang and T. Uemura, *Chem. Soc. Rev.*, 2017, **46**, 3108–3133.
24 S. Zhao, X. Cao, Z. Ma, Z. Wang, Z. Qiao, J. Wang and S. Wang, *Ind. Eng. Chem. Res.*, 2015, **54**, 5139–5148.
25 G. Huang, Q. H. Yang, Q. Xu, S. H. Yu and H. L. Jiang, *Angew. Chem., Int. Ed.*, 2016, **55**, 7505–7509.
26 H. Ren, L. Zhang, J. An, T. Wang, L. Li, X. Si, L. He, X. Wu, C. Wang and Z. Su, *Chem. Commun.*, 2014, **50**, 1000–1002.
27 J. H. Gu, H. W. Fan, C. X. Li, J. Caro and H. Meng, *Angew. Chem., Int. Ed.*, 2019, **58**, 5297–5301.
28 G. H. Yang, D. Q. Zhang, G. Zhu, T. R. Zhou, M. T. Song, L. L. Qu, K. C. Xiong and H. T. Li, *RSC Adv.*, 2020, **10**, 8540–8547.
29 R. Heu, M. Ateia and C. Yoshimura, *Catalysts*, 2020, **10**, 711.
30 K. Jayaramulu, K. K. Datta, C. Rosler, M. Petr, M. Otyepka, R. Zboril and R. A. Fischer, *Angew. Chem., Int. Ed.*, 2016, **55**, 1178–1182.
31 Z. Z. Yang, Q. B. Zheng, H. X. Qiu, J. Li and J. H. Yang, *Carbon*, 2015, **86**, 372.
32 L. A. Shi, J. Ge, B. C. Hu, T. Ma, H. Y. Zhao, Y. H. Song, C. Li and S. H. Yu, *Nano Res.*, 2021, **14**, 2697–2702.
33 T. C. Sun, S. Hao, R. Q. Fan, M. Y. Qin, W. Chen, P. Wang and Y. L. Yang, *ACS Appl. Mater. Interfaces*, 2020, **12**, 56435–56444.
34 M. Qin, Y. Xu, R. Cao, W. Feng and L. Chen, *Adv. Funct. Mater.*, 2018, **28**, 1805053.
35 J. Ge, L. A. Shi, Y. C. Wang, H. Y. Zhao, H. B. Yao, Y. B. Zhu, Y. Zhang, H. W. Zhu, H. A. Wu and S. H. Yu, *Nat. Nanotechnol.*, 2017, **12**, 434–440.
36 Y. Wang, Y. Yu, R. Li, H. J. Liu, W. Zhang, L. J. Ling, W. B. Duan and B. Liu, *J. Mater. Chem. A*, 2017, **5**, 20136–20140.
37 D. Li, M. B. Muller, S. Gilje, R. B. Kaner and G. G. Wallace, *Nat. Nanotechnol.*, 2008, **3**, 101–105.
38 L. G. Guex, B. Sacchi, K. F. Peuvot, R. L. Andersson, A. M. Pourrahimi, V. Strom, S. Farris and R. T. Olsson, *Nanoscale*, 2017, **9**, 9562–9571.
39 R. N. Wenzel, *Ind. Eng. Chem.*, 1936, **20**, 988–994.
40 L. Wen, Y. Tian and L. Jiang, *Angew. Chem., Int. Ed.*, 2015, **54**, 3387–3399.
41 A. Li, H. X. Sun, D. Z. Tan, W. J. Fan, S. H. Wen, X. J. Qing, G. X. Li, S. Y. Li and W. Q. Deng, *Energy Environ. Sci.*, 2011, **4**, 2062–2065.
42 G. H. Jiang, R. B. Hu, X. G. Xi, X. H. Wang and R. J. Wang, *J. Mater. Res.*, 2013, **28**, 651–656.
43 W. W. Lei, D. Portehault, D. Liu, S. Qin and Y. Chen, *Nat. Commun.*, 2013, **4**, 1777.
44 C. H. Lee, N. Johnson, J. Drelich and Y. K. Yap, *Carbon*, 2011, **49**, 669–676.

45 Z. G. Xu, Y. Zhao, H. X. Wang, H. Zhou, C. X. Qin, X. G. Wang and T. Lin, *ACS Appl. Mater. Interfaces*, 2016, **8**, 5661–5667.
46 L. Zhang, Z. Zhang and P. Wang, *NPG Asia Mater.*, 2012, **4**, e8.
47 H. G. Zhu, S. Yang, D. Y. Chen, N. J. Li, Q. F. Xu, H. Li, J. H. He and J. M. Lu, *Adv. Mater. Interfaces*, 2016, **3**, 1500683.
48 Z. G. Xu, Y. Zhao, H. X. Wang, X. G. Wang and T. Lin, *Angew. Chem., Int. Ed.*, 2015, **54**, 4527–4530.
49 D. Kim, D. W. Kim, O. Buyukcakir, M.-K. Kim, K. Polychronopoulou and A. Coskun, *Adv. Funct. Mater.*, 2017, **27**, 1700706.
50 W. F. Zhang, N. Liu, Q. D. Zhang, R. X. Qu, Y. N. Liu, X. Y. Li, Y. Wei, L. Feng and L. Jiang, *Angew. Chem., Int. Ed.*, 2018, **57**, 5740–5745.